nature catalysis

Supplementary information

https://doi.org/10.1038/s41929-024-01177-6

Exploring mesoscopic mass transport effects on electrocatalytic selectivity

In the format provided by the authors and unedited

Contents

Supplementary Methods

Microkinetic mean field model

Our microkinetic mean field model (mkm) consists of a minimal reaction network to represent the desorption–re-adsorption–reaction mechanism. The reaction network is based on the model intermediates A*, B*, C*, and D* as depicted in Supplementary Figure. 1 and can be summarized via six elementary reaction steps:

$$\mathrm{A_g} + {}^* \rightleftharpoons \mathrm{A^*} \tag{1}$$

$$\mathrm{A^*} + \mathrm{H^+} + \mathrm{e^-} \overset{\alpha=0.5}{\rightleftharpoons} \mathrm{B^*} \tag{2}$$

$$\mathrm{B^*} + \mathrm{H^+} + \mathrm{e^-} \overset{\alpha=0.5}{\rightleftharpoons} \mathrm{C^*} \tag{3}$$

$$\mathrm{C^*} \rightleftharpoons \mathrm{C_{aq}} \tag{4}$$

$$\mathrm{C^*} + \mathrm{H^+} + \mathrm{e^-} \overset{\alpha=0.5}{\rightleftharpoons} \mathrm{D^*} \tag{5}$$

$$\mathrm{D^*} \rightleftharpoons \mathrm{D_g} + {}^* \tag{6}$$

where Supplementary Equations 1, 4, and 6 are elementary reactions with potential independent adsorption/desorption steps while 2, 3, and 5 are electrochemical steps which are here shown as reduction processes adding a proton $\mathrm{H^+}$ and electron $\mathrm{e^-}$. The selectivity is determined via the competition of step 4, where the intermediate C* can desorb to $\mathrm{C_{aq}}$ and step 5, where C* is further reduced to D*. The elementary reactions 1, 2, 3, and 6 are preceding and subsequent reaction steps embedding the selectivity determining steps (SDS). The reaction network can be altered to include the direct reduction of B* to $\mathrm{C_{aq}}$ which replaces 3 with:

$$\mathrm{B^*} + \mathrm{H^+} + \mathrm{e^-} \overset{\alpha=0.5}{\rightleftharpoons} \mathrm{C_{aq}} + {}^*. \tag{7}$$

This reaction alters the SDS and has been suggested for acetate in $\mathrm{CO_2RR}$[1]. Replacing 3 with 7 leads to a quantitatively identical behavior in the showcase studies presented in the main text (disregarding numerical imprecision). However, a qualitative difference between Supplementary Equations 3 and 7 is found for large values of the desorption barrier $\Delta G^{\ddagger}_{\mathrm{des}}$ as demonstrated in Supplementary Figure 2 (tagged as model b). These large values are, however, irrelevant for the discussed desorption–re-adsorption–reaction mechanism since they eliminate any selectivity and lead to either the complete conversion or desorption of the volatile species $\mathrm{C_{aq}}$ giving a selectivity for $\mathrm{C_{aq}}$ of 0 % and 100 %, respectively. Note, that we included step 3 in the embedding reactions only for the purpose to be replaced by step 7, since step 3 is otherwise redundant.

The reaction barriers of the elementary reactions 1, 2, 3, (7), and 6 are left unaltered for all simulations in this work, while decisive barriers occurring in the SDS are varied as indicated in Supplementary Table 1 and further discussed in the main text and below (see Parameter sensitivity analysis). All fixed reaction barriers at $U_{\mathrm{SHE}} = 0$ are listed in Supplementary Table 1. The fixed barriers are chosen in a way to render the SDS pivotal for selectivity in the reaction kinetics. In that, the SDS are subsequent to the rate determining step

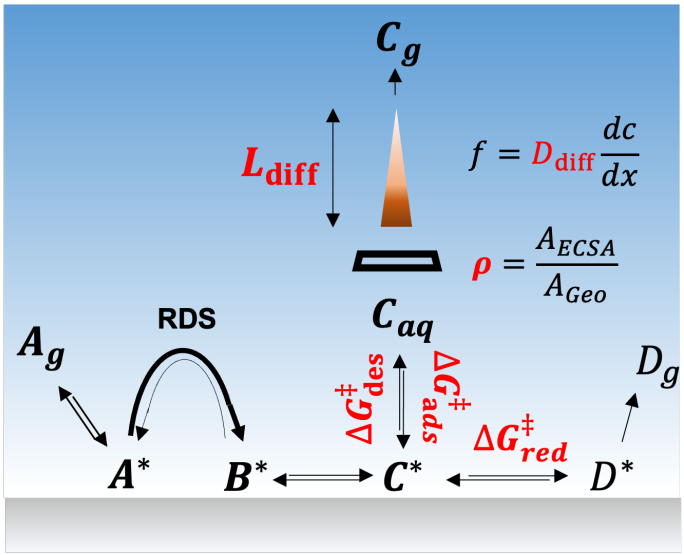

Supplementary Figure 1: Schematic of the employed multi-scale model. Shown is the simple reaction network used in our mkm to describe the representative surface reaction steps as well as the diffusion of C_g described by mass transport. The key parameters influencing the selectivity of the desorption–re-adsorption–reaction mechanism are labelled in the network and marked in red.

(RDS) in Supplementary Equation 2 which is adjusted to yield typical current densities[1]. Additionally, the adsorption/desorption equilibrium for the reactant species A* is chosen to yield a coverage of $\theta_{A^*} \approx 0.25$ which is a typical value when including lateral adsorbate-adsorbate interactions[2]. The latter are not specifically included here. We note, that choosing a different adsorption/desorption equilibrium for A* would lead to a lower or higher coverage, and quantitatively affect the influence of SDS-related desorption and adsorption barriers of species C on the selectivity ($\Delta G^{\ddagger}_{\mathrm{des}}$ and $\Delta G^{\ddagger}_{\mathrm{ads}}$ in Supplementary Table 1). This quantitative influence follows the relation of the adsorption rate, coverage, and rate constant as $r_{\mathrm{ads}} \propto \theta^* \cdot k_{\mathrm{ads}}$, shifting the curves in Supplemental Figure 2 (a), and (b) along the x-axis and thus yield the same qualitative picture. All backwards reaction barriers in Supplementary Equation 2, 5, 6 are chosen to render the corresponding steps irreversible. The dependence of the electrochemical reaction barriers in Supplementary Equation 2, 3, (7), and 5 on applied potential was determined on basis of the computational hydrogen electrode (CHE)[3] and a transfer coefficient α of 1/2[4].

Supplementary Table 1: Reaction barriers in [eV] at $U_{\mathrm{SHE}} = 0$ used in the mkm, labelled as forward (fwd) and backward (bwd) for each reaction step. Parameters that affect the SDS are varied throughout this work and are marked as $\Delta G^{\ddagger}_{\mathrm{des}}$, $\Delta G^{\ddagger}_{\mathrm{ads}}$, and $\Delta G^{\ddagger}_{\mathrm{red}}$

	1	2	7 / 3	4	5	6
$\Delta G^{\ddagger}_{\mathrm{fwd}}$	0.027	1.45	1.25	$\Delta G^{\ddagger}_{\mathrm{des}}$	$\Delta G^{\ddagger}_{\mathrm{red}}$	0.0
$\Delta G^{\ddagger}_{\mathrm{bwd}}$	0.0	1.46	1.56	$\Delta G^{\ddagger}_{\mathrm{ads}}$	$\Delta G^{\ddagger}_{\mathrm{red}} + 0.55$	0.44

On basis of the reaction network described by the Supplementary Equations 1-6 we formulate the time-

dependent coupled differential equations making up the mkm:

$$\frac{d\theta_{\mathrm{A}^*}}{dt} = k_{\mathrm{A}^*\leftarrow\mathrm{A_g}} \cdot \theta^* \cdot a_{\mathrm{A_g}} - k_{\mathrm{A_g}\leftarrow\mathrm{A}^*} \cdot \theta^{\mathrm{A}} + k_{\mathrm{A}^*\leftarrow\mathrm{B}^*}(U) \cdot \theta^{\mathrm{B}} - k_{\mathrm{B}^*\leftarrow\mathrm{A}^*}(U) \cdot \theta^{\mathrm{A}} \tag{8}$$

$$\frac{d\theta_{\mathrm{B}^*}}{dt} = k_{\mathrm{B}^*\leftarrow\mathrm{A}^*}(U) \cdot \theta^{\mathrm{A}} - k_{\mathrm{A}^*\leftarrow\mathrm{B}^*}(U) \cdot \theta^{\mathrm{B}} + k_{\mathrm{B}^*\leftarrow\mathrm{C}^*}(U) \cdot \theta^{\mathrm{C}} - k_{\mathrm{C}^*\leftarrow\mathrm{B}^*}(U) \cdot \theta^{\mathrm{B}} \tag{9}$$

$$\begin{aligned}\frac{d\theta_{\mathrm{C}^*}}{dt} &= k_{\mathrm{C}^*\leftarrow\mathrm{B}^*}(U) \cdot \theta^{\mathrm{B}} - k_{\mathrm{B}^*\leftarrow\mathrm{C}^*}(U) \cdot \theta^{\mathrm{C}} + k_{\mathrm{C}^*\leftarrow\mathrm{D}^*}(U) \cdot \theta^{\mathrm{D}} - k_{\mathrm{D}^*\leftarrow\mathrm{C}^*}(U) \cdot \theta^{\mathrm{C}} \\ &\quad + k_{\mathrm{C}^*\leftarrow\mathrm{C_{aq}}} \cdot \theta^* \cdot a_{\mathrm{C_{aq}}} - k_{\mathrm{C_{aq}}\leftarrow\mathrm{C}^*} \cdot \theta^{\mathrm{C}}\end{aligned} \tag{10}$$

$$\frac{d\theta_{\mathrm{D}^*}}{dt} = k_{\mathrm{D}^*\leftarrow\mathrm{C}^*}(U) \cdot \theta^{\mathrm{C}} - k_{\mathrm{C}^*\leftarrow\mathrm{D}^*}(U) \cdot \theta^{\mathrm{D}} - k_{\mathrm{D_g}\leftarrow\mathrm{D}^*} \cdot \theta^{\mathrm{D}} + k_{\mathrm{D}^*\leftarrow\mathrm{D_g}} \cdot \theta^* \cdot a_{\mathrm{D_g}} \tag{11}$$

where θ^i is the coverage, a_i is the activity of species i, and $k_{j\leftarrow i}$ is the rate constant for the reaction $i \rightarrow j$, note that (U) indicates a potential dependence of the rate constant according to the procedure described above.

Supplementary Equations 8-11, are solved for the steady-state condition $\frac{d\theta^i}{dt} = 0$ via a mean field approach using an ODE solver as available in Scipy[5]. The rate constants $k_{j\leftarrow i}$ for each elementary process are given by the Arrhenius equation $k_{ij} = Ae^{-\frac{\Delta G_a^{i\leftarrow j}}{k_{\mathrm{B}}T}}$. Here, ΔG_a represents the activation energy, k_{B} the Boltzmann constant, T the temperature, and the prefactor is $A = k_{\mathrm{B}}T/\hbar = 10^{-13}\ \mathrm{s}^{-1}$.

Coupling diffusion to the microkinetic model

The one dimensional diffusion of intermediate C_{aq} is analytically described via Fick's first law:

$$f_{\mathrm{diff}} = D_{\mathrm{diff}} \cdot \frac{\Delta c}{L_{\mathrm{diff}}} \tag{12}$$

where f_{diff} is the diffusion flux, D_{diff} the diffusion coefficient, Δc the concentration difference, and L_{diff} the diffusion length. This simple expression is valid at steady state[6] which we exclusively consider in this case study. D_{diff} and L_{diff} are case specific parameters that are chosen as described in Supplementary Table 2 while f_{diff} and Δc are solved in conjunction with the flux of the mkm.

The microkinetic model and the diffusion equation are iteratively solved to align the flux f of the volatile species $\mathrm{C_{aq}}$ in both descriptions. f_{mkm} corresponds to the net outward flux (desorption minus adsorption of $\mathrm{C_{aq}}$) in the microkinetic model and the solution to Supplementary Equation 12, respectively, which follows the general expression:

$$\begin{aligned}\rho \cdot f_{\mathrm{mkm}} &= \rho \cdot \left(-k_{\mathrm{C}^*\leftarrow\mathrm{C_{aq}}} \cdot \theta^* \cdot a_{\mathrm{C_{aq}}} + k_{\mathrm{C_{aq}}\leftarrow\mathrm{C}^*} \cdot \theta^{\mathrm{C}}\right) \\ &= a_{\mathrm{C_{aq}}} \cdot H_{\mathrm{s}}^{cp} \cdot \frac{D_{\mathrm{diff}}}{L_{\mathrm{diff}}} = c^{\mathrm{C_{aq}}}(x=0) \cdot \frac{D_{\mathrm{diff}}}{L_{\mathrm{diff}}} = f_{\mathrm{diff}}\end{aligned} \tag{13}$$

In practice we optimize the activity/interfacial concentration of $\mathrm{C_{aq}}$ ($c^{\mathrm{C_{aq}}}(x=0)$) for the microkinetic model and diffusion equation until the fluxes align. The roughness ρ is used to relate the fluxes of the surface reaction and transport which are proportional to the active surface area A_{ECSA} of the catalyst and to the geometric area A_{Geo}, respectively. The bulk concentration of the product or intermediate $\mathrm{C_{aq}}$, presents a boundary condition

and is set to zero thus changing the term Δc in Supplementary Equation 12 to the interfacial concentration $c^{\mathrm{C_{aq}}}(x=0)$. We convert the interfacial concentration $c^{\mathrm{C_{aq}}}(x=0)$ of $\mathrm{C_{aq}}$ obtained from the diffusion equation 12 to an activity for the microkinetic model used in Supplementary Equation 4 via a Henry's law constant (compare Supplementary Table 2).

Parameter sensitivity analysis

Six parameters are decisive for the selectivity of the "desorption–re-adsorption–reaction" mechanism which we can individually investigate in our multi-scale model. In the microkinetic model the relevant barriers affecting the volatile species $\mathrm{C^*/C_{aq}}$ include its desorption $\Delta G^{\ddagger}_{\mathrm{des}}$, adsorption $\Delta G^{\ddagger}_{\mathrm{ads}}$, and reduction $\Delta G^{\ddagger}_{\mathrm{red}}$ (compare Supplementary Table 1). Since all products are in equilibrium at steady state, the desorption-adsorption energetics are more illustratively described by the adsorption free energy ΔG_{ads} $(= \Delta G^{\ddagger}_{\mathrm{ads}} - \Delta G^{\ddagger}_{\mathrm{des}})$ on the one hand, and the desorption barrier $\Delta G^{\ddagger}_{\mathrm{des}}$ in competition with the effective reduction barrier $\Delta G^{\ddagger}_{\mathrm{red}}(U,\alpha)$ on the other. The latter depends on the applied potential U_{SHE} and the transfer coefficient α which yield correlated selectivity trends, in the main text we therefore only discuss the potential dependence with U_{SHE}. For the diffusion model, the diffusion coefficient D_{diff}, the diffusion length L_{diff} and the roughness ρ are decisive.

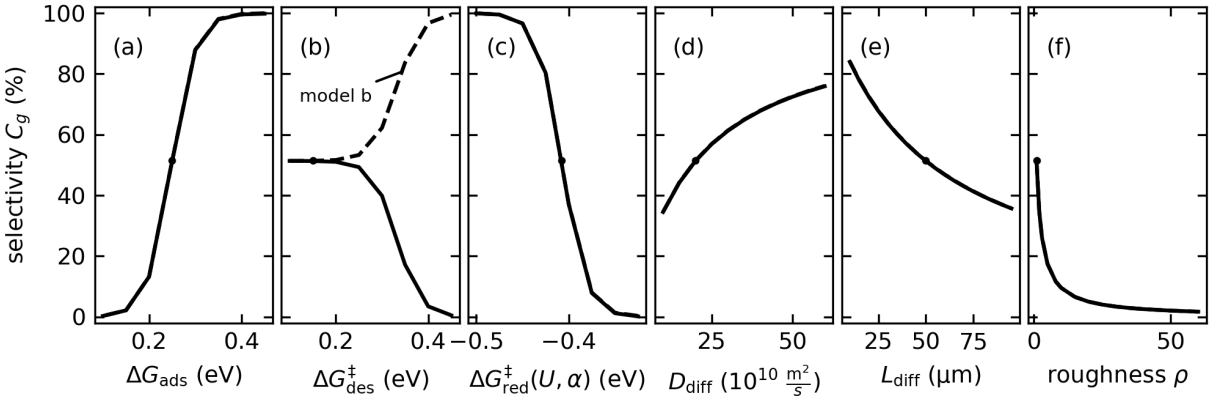

Supplementary Figure 2: Selectivity for the volatile product C_g against all selectivity determining parameters influencing the desorption–re-adsorption–reaction mechanism in our multi-scale model. For each parameter, a range is screened while the other parameters are held at a default value (marked with a dot). The parameter ranges are chosen to either capture the relevant selectivity changes in the case of reaction energies or are chosen within physically reasonable ranges in case of the transport parameters. The dashed line labeled model b represents the multi-scale model using an mkm with Supplementary Equation 7 which only shows diverging behavior for large values of $\Delta G^{\ddagger}_{\mathrm{des}}$.

The effective selectivity behavior of the model is depicted in Supplementary Figure 2. The surface reaction energies which are depicted in panel a-c have an expectedly strong effect on the selectivity following their exponential dependence[7] on the reaction rate and yield a 0-100 % selectivity change within a 0.2 eV range. We find that the effect of $\Delta G^{\ddagger}_{\mathrm{des}}$ depends on the assumed reaction mechanism, based on Supplementary Equation 3 or 7 as discussed in the Microkinetic mean field model section, where each reaction leads to an opposite behavior of the selectivity for C_g with an increasing desorption barrier $\Delta G^{\ddagger}_{\mathrm{des}}$. A diverging selectivity behavior is, however, only seen for large desorption barriers $\Delta G^{\ddagger}_{\mathrm{des}}$ >0.2 eV.

The influence of the diffusion related parameters are shown within physically reasonable ranges in panel

d-f in Supplementary Figure 2. It can be seen that all these parameters decisively influence the selectivity as well, albeit to a lesser extent. Within typical parameter ranges which can be expected in experiment, only the catalyst roughness ρ shows a dramatic influence. This is due to the fact that a change of $\rho = 1$ on a truly planar surface to a tortuous surface $\rho >> 1$ is easily realized. On the other hand, the diffusion coefficient and diffusion length can only be moderately influenced: Depending on the solute, typical ranges for the diffusion coefficient are within 1.5-2.5 $\cdot 10^{-10} \mathrm{m^2 s^{-1}}$ which can affect selectivity within 20 % (see Supplementary Figure 2), exceptions are inert or small gases as well as H^+ and OH^- which can undergo the Grotthuss mechanism. Similar to the diffusion coefficient, the diffusion length is typically between 20 and 70 μm, as estimated for rotating ring-disc electrodes (RRDEs) by the Koutecký-Levich equation[8]. The diffusion length can be varied in special reactor setups and this has been demonstrated to lead to significant selectivity changes of up to e.g. 40 % towards the volatile CO product during the CO_2RR on Cu[9,10]. To demonstrate this effect for another system, we analyzed experimental RRDE data for ORR at Pt(111) by Marković *et al.*[11]. We specifically used the analytical solution proposed by Damjanovic *et al.*[12] which characterizes the selectivity towards the volatile H_2O_2 by relating the disk over ring current ratio ($I_{\mathrm{disk}}/I_{\mathrm{ring}}$) to the rotation rate ω. At the higher 0.2V potential, Supplementary Figure 3 shows very little variation in $I_{\mathrm{disk}}/I_{\mathrm{ring}}$ as the angular velocity (ω) is changed. This suggests little effect from the desorption-re-adsorption-reaction mechanism, possibly due to a dominating ORR mechanism that directly forms H_2O without going through an H_2O_2 intermediate. This hypothesis is supported by the low I_{ring} values measured within the higher potential range, showing negligible H_2O_2 reduction at the ring[11]. At more reducing potentials (< 0.2 V) where more H_2O_2 is formed, however, a linear relationship between $I_{\mathrm{disk}}/I_{\mathrm{ring}}$ and $\omega^{-1/2}$ is observed. This relationship suggests that H_2O_2 diffusion changes the ORR selectivity, as expected from the desorption-re-adsorption-reaction mechanism. It is unclear whether the small spread in the value of the y-axis intercept is due to noise in the experimental data or competing ORR pathways. The complex potential dependance of the ORR mechanism over Pt has been previously reported and is in line with our discussion in section Data sets for ORR and MOR. Regardless of this complexity, however, the demonstrated selectivity dependence upon rotation rate within the RRDE setup directly corroborates the desorption-re-adsorption-reaction mechanism.

In the main text we focus our discussion on how the selectivity for the volatile species C_g is affected by the potential U_{SHE} and the roughness ρ. For a quantitative understanding of the selectivity dependence on these parameters we formulate the analytical expressions 14 and 15. The dependence of the selectivity of C_{aq} on U_{SHE} follows the competition between the reduction and desorption flux of C^* (ignoring re-adsorption contribution), f_{red} and f_{des}, respectively:

$$
\begin{aligned}
f_{\mathrm{red}} &= \rho \cdot \frac{1}{A_{\mathrm{site}}} \cdot \theta_{C^*} \cdot \exp - \frac{\Delta G^{\ddagger}_{\mathrm{red}}(U)}{k_{\mathrm{B}} T} \\
f_{\mathrm{des}} &= \rho \cdot \frac{1}{A_{\mathrm{site}}} \cdot \theta_{C^*} \cdot \exp - \frac{\Delta G^{\ddagger}_{\mathrm{des}}}{k_{\mathrm{B}} T} \\
S(\mathrm{C_g}) \propto \frac{f_{\mathrm{des}}}{f_{\mathrm{red}}} &= \exp\left(- \frac{\Delta G^{\ddagger}_{\mathrm{des}} - \Delta G^{\ddagger}_{\mathrm{red}}(U)}{k_{\mathrm{B}} T} \right).
\end{aligned}
\tag{14}
$$

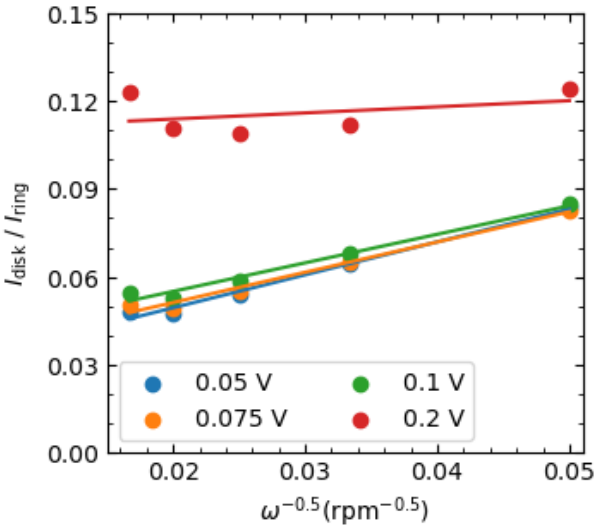

Supplementary Figure 3: Ratio of disc over ring currents ($I_{\text{disk}}/I_{\text{ring}}$) as a function of $\omega^{-1/2}$ where ω is the rotation rate in an RRDE setup. The experimental data were adapted from Marković *et al.*[11] for the ORR on Pt(111) at different potentials (according to the figure's label) in 0.1M KOH and analyzed using the solution proposed in Ref. [12].

where the $\rho \cdot \frac{1}{A_{\text{site}}}$ is the product of the roughness with the area per active site which scales the area dependence of surface reactions. Supplementary Equation 14 illustrates a strong exponential effect of U_{SHE} on the selectivity. The selectivity dependence of C_{aq} on the roughness ρ follows the competition between the adsorption flux f_{ads} and the combined desorption f_{des} and diffusion flux f_{diff}. A selectivity expression follows as:

$$
\begin{aligned}
f_{\text{ads}} &= \rho \cdot \frac{1}{A_{\text{site}}} \cdot \theta^* \cdot H_{\text{s}}^{cp,\text{C}_{\text{aq}}} \cdot c^{\text{C}_{\text{aq}}}(x=0) \cdot \exp -\frac{\Delta G_{\text{ads}}^{\ddagger}}{k_{\text{B}}T} \\
f_{\text{diff}} &= c^{\text{C}_{\text{aq}}}(x=0) \cdot D_{\text{diff}}/L_{\text{diff}} \\
S(\text{C}_{\text{g}}) &= \frac{f_{\text{diff}}}{f_{\text{ads}} - f_{\text{des}}} = \frac{c^{\text{C}_{\text{aq}}}(x=0) \cdot D_{\text{diff}}/L_{\text{diff}}}{R} \propto \frac{1}{\rho} \\
R &= H_{\text{s}}^{cp,\text{C}_{\text{aq}}} \cdot c^{\text{C}_{\text{aq}}}(x=0) \cdot \frac{1}{A_{\text{site}}} \cdot \rho \cdot \theta^* \cdot \exp\left(-\frac{\Delta G_{\text{ads}}^{\ddagger}}{k_B T}\right) - \frac{1}{A_{\text{site}}} \cdot \rho \cdot \theta^c \cdot \exp\left(-\frac{\Delta G_{\text{des}}^{\ddagger}}{k_B T}\right) \\
&= \frac{1}{A_{\text{site}}} \cdot \rho \cdot \left(H_{\text{s}}^{cp,\text{C}_{\text{aq}}} \cdot c^{\text{C}_{\text{aq}}}(x=0) \cdot \theta^* \cdot \exp\left(-\frac{\Delta G_{\text{ads}}^{\ddagger}}{k_B T}\right) - \theta^c \cdot \exp\left(-\frac{\Delta G_{\text{des}}^{\ddagger}}{k_B T}\right)\right)
\end{aligned}
\tag{15}
$$

where $c^{\text{C}_{\text{aq}}}(x=0)$ is the interfacial concentration and $H_s^{cp,\text{C}_{\text{aq}}}$ the Henry constant of the volatile species C. The final expression in Supplementary Equation 15 reveals the $\frac{1}{\rho}$ dependency in selectivity.

Model parameters for the presented showcase studies

In the main text we use our coupled microkinetic and 1D transport model to reproduce experimental data for the selectivity of H_2O_2 in ORR, formaldehyde in MOR, as well as CO and acetaldehyde in CO_2RR. For these test cases, we adjust the decisive parameters in the SDS and diffusion part according to literature values and best guesses if data is not available (by fitting to experiment), all parameters are listed in Supplementary Table 2. We note that, generally, no data was available for the adsorption/desorption thermodynamics with the

exception of CO (where we chose values of the more abundant Cu(111) facets)[13]. The latter does, however, not account for competitive adsorption[14] or field effects[4,15–17] which may influence CO's stability on the surface.

To describe the selectivity of acetate (Ac, H_3CCOO^-) in CO_2RR (Fig. 4 in the main text), we adopt our recently published model of a transport and solution reaction mediated mechanism[1]. For this model the reaction pathway to the volatile species ketene (that is converted to acetate in solution) was fully explored using elaborate *ab initio* methods. From these calculations all relevant surface reaction barriers are provided. Equally, all necessary transport related parameters are availabel in literature with the exception of H_s^{cp} for the volatile species ketene, which was indirectly fit to experiment.

Supplementary Table 2: Parameters used in the coupled microkinetic and 1D transport model. Given are the numbers for the Henry's law solubility constant (pressure / concentration) H_s^{cp}, the diffusion coefficient D_{diff}, the desorption thermodynamics ΔG_{des}, the desorption barrier $\Delta G_{des}^{\ddagger}$, and the reduction barrier $\Delta G_{red}^{\ddagger}$ as described above. In all examples a diffusion length L_{diff} of 50 μm is used, which presents a realistic diffusion length as estimated by the Koutecký-Levich equation[8]. Values in *italic* have been estimated since literature values were not available.

	H_s^{cp} [atm l mol^{-1}]	D_{diff} [m^2 s^{-1}]	ΔG_{ads} [eV]	$\Delta G_{des}^{\ddagger}$ [eV]	$\Delta G_{red}^{\ddagger}$ [eV]
H_2O_2	1.20e-05[18]	15.6e-10[19]	*-0.1*	0.2[20]	*1.1*
CH_2O	1.99e-4[21]	17.541e-10[22]	*0.0*	*0.165*	*1.1*
CO	1100[23]	20.3e-10[6]	-0.1[13]	*0.165*	1.5[1]*
MeCHO	0.0759[24]	13.75e-10[25]	*0.14*	*0.165*	*0.96*
Ac	see model details in [1]				

* slightly adapted from 1.45 eV used in [1]

Supplementary Note 1

Definition of selectivity against later redox products

The discussed (and displayed) selectivity in the main text describes the SDS of the desorption–re-adsorption–reaction. This selectivity is defined as the selectivity of the volatile product (e.g. hydrogen peroxide, formaldehyde, carbon monoxide, acetaldehyde, or acetate) against products which result from its further reduction or oxidation. This definition of selectivity is inherent in our simplified model which only describes said mechanism. However, experimental data can also include other products, resulting from competition of other side and parasitic products that do not derive from the volatile product, e.g. hydrogen in CO_2RR.

For the shorter reaction networks like the ORR (hydrogen peroxide, H_2O_2) and MOR (formaldehyde, CH_2O) the selectivity S relevant to the here discussed SDS corresponds to the total reaction selectivity, following the fraction of different product fluxes f as

$$S_{H_2O_2} = \frac{f_{H_2O_2}}{f_{H_2O_2} + f_{H_2O}} = \frac{f_{H_2O_2}}{f_{tot}} \tag{16}$$

$$S_{H_2CO} = \frac{f_{H_2CO}}{f_{H_2CO} + f_{HCOOH} + f_{CO_2}} = \frac{f_{H_2CO}}{f_{tot}}. \tag{17}$$

For the products carbon monoxide (CO), acetate (Ac, H_3CCOO^-), and acetaldehyde (MeCHO) evaluated in the

significantly more complex CO_2RR reaction, the relevant selectivities are described by the following relations

$$S_{\mathrm{CO}} = \frac{f_{\mathrm{CO}}}{f_{\mathrm{CO}} + f_{\mathrm{C_1}} + f_{\mathrm{C_{2+}}} \cdot n_{\mathrm{C}}(\mathrm{C_{2+}})} \tag{18}$$

$$S_{\mathrm{Ac}} = \frac{f_{\mathrm{Ac}}}{f_{\mathrm{C_{2+}}}} \tag{19}$$

$$S_{\mathrm{MeCHO}} = \frac{f_{\mathrm{MeCHO}}}{f_{\mathrm{C_{2+}}}} \tag{20}$$

where the C_1 products include methane, and methanol, and the C_{2+} products include ethylene, ethanol, acetate, n-propanol, and the less abundant[26] acetaldehyde, ethane, glycolaldehyde, ethylene-glycol, allyl-alcohol, propionaldehyde, acetone, hydroxyacetone, if detected. In Supplementary Equation 18 the C_{2+} flux $f_{C_{2+}}$ is normalized by the number of carbons $n_C(C_{2+})$ contained in each C_{2+} product to properly account for the mass balance in respect to CO.

In most literature data, the molar fluxes f_p for a product p are not reported. For this reason, we approximate them from the experimental partial current densities j_p or Faradaic efficiencies (FE) and the product specific number of redox steps n_p^{el} as

$$f_p \propto j_p/n_p^{\mathrm{el}} = (FE \times j_{\mathrm{tot}}/n_p^{\mathrm{el}}). \tag{21}$$

and approximate uncertainties for the estimated selectivities S in our analysis (see provided Supplementary Data) by means of error propagation (if applicable).

Estimation of the catalyst roughness from measured current density

For some displayed experimental data sets no capacitance measurements are provided to determine the catalyst roughness and for others these roughness values appear inconsistent, e.g. for Cu-Pd alloys (see main text and the Data sets on Ac selectivity during CORR section). In these cases, we evaluated the roughness (or ECSA) from the total current densities.

The roughness is estimated by fitting the experimentally measured total current densities (j_{tot}) and the corresponding applied potential (U_{SHE}). We use an exponential function $j_{\mathrm{tot}}(U_{\mathrm{SHE}}) = a \cdot \exp(b * U_{\mathrm{SHE}})$, where a, b are fitting parameters. Since compared data sets are taken at the same pH (see Data sets on Ac selectivity during CORR Section), the use of U_{SHE} or U_{RHE} is equivalent. In a first step each catalysts' total current vs potential data set is fitted individually to determine the individual parameter sets. The parameter b is related to the Tafel slope which we assume constant at comparable electrochemical conditions[27,28]. Following this argument, we subsequently re-fit all data sets with all the different parameters b which yields a range of intercepts a for each data set. From this range of a we determine a mean and standard deviation (e.g. see Supplementary Table 3). The determined intercept a compares the activity at the same potential $U_{\mathrm{SHE}} = 0$ and is therefore a reliable, relative measure of the roughness. A script for the described roughness estimation routine is available via the link provided in the Code availability statement.

Supplementary Note 2

Data sets for ORR and MOR

For the ORR measurements presented in the main text, we do not discuss the potential dependence of the H_2O_2 selectivity. In general the potential dependence of this selectivity is highly complex and differs strongly between catalysts and facets[20]. This is also true for the data collected by Behm *et al.*[29], which does not reflect the potential dependent selectivity generalized in this work for the desorption–re-adsorption–reaction. It is likely that this is due to competing reaction pathways which not all involve H_2O_2 as a volatile intermediate. We note, however, that the roughness dependence can be found at the different potentials investigated in the experiments as shown in Supplementary Figure 4a, which demonstrates that H_2O_2 is always subject to the desorption-diffusion-re-adsorption mechanism. These ORR data are obtained from a flow cell setup during potentiodynamic measurements in the potential range of 0.06 to 1.16 V vs. RHE at a sweep rate of 10 mV/s and in 0.5 M sulfuric acid (pH 0.13) with dynamic product detection.

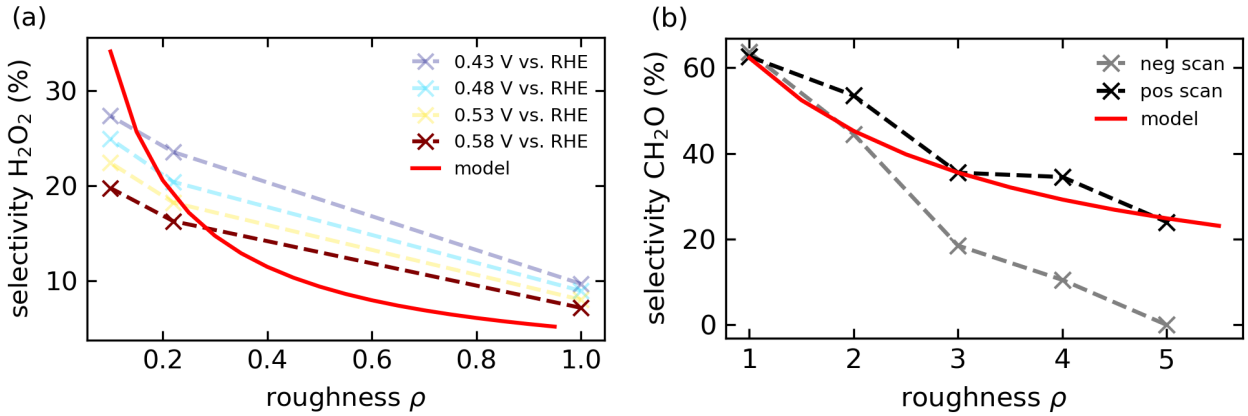

Supplementary Figure 4: Selectivity for (a) H_2O_2 during ORR and (b) CH_2O during MOR against roughness ρ of Pt, adapted from [29] and [30], respectively and analog to the main text. In comparison to the main text, we added selectivity data taken at different potentials for the ORR and added the CH_2O selectivity resulting from the negative going scan.

The MOR data is obtained from potentiodynamic measurements, hence through product collection after positive or negative going potential scans[30]. These scans were conducted at a range of 0.16 to 1.16 V vs. RHE at a sweep rate of 10 mV/s and in 0.5 M sulfuric acid (pH 0.13). The transient mode of product collection which makes any potential dependency analysis impossible. The resulting selectivity to roughness trends, shown in Supplementary Figure 4b, reveal an almost quantitative agreement when comparing to the positive going scan but deviate in the case of the negative scan (not shown in the main text). This deviation may be attributed to the surface oxidation of the Pt catalyst after the positive going scan (evidenced by a hysteresis of associated CVs[30]) which may affect surface reactivity during the negative scan.

Data sets on CO & MeCHO selectivity during CO_2RR

The data sets in Figure 3a in the main text, showing the selectivity of CO, are all based on comparable experiments in an H-cell setup in an 0.1 M $KHCO_3$ electrolyte[26,31,32]. The similar setup of these experiments

likely enables their direct comparison. Catalyst roughness values for the data from [32] are estimated via the total current density (see section on Estimation of the catalyst roughness from measured current density) since no values by capacitance measurements are available. The fitting procedure was limited to current densities $\leq 10\text{mA/cm}^2$ due to underlying transport limitations at high current densities in the H-cell setup. We exclude the Cu(100) and Cu(110) single crystal data from [32] which appear rougher by a factor of 1.4 compared to the Cu(111) single crystal and remark the OD-Cu roughness was detemined with a comparably high uncertainty as $\rho = 16.3 \pm 7.4$. The roughness value for OD-Cu from [31] is taken based on the authors and our total current density estimates of $\rho = 30$ instead of the authors measured $\rho = 475$ via capacitance measurements. In Fig. 1 in [31], it can be seen that the OD-Cu catalyst is heavily evolving during the first hours of electrolysis and the average reported current densities rather fit to the long term estimate than to the as-prepared catalyst which most likely was used for the capacitance measurements.

The data sets adapted from [33–35] in Figure 3b in the main text, which we use to show the selectivity of acetaldehyde, are all based on experiments conducted for direct CO reduction in a CO sparged H-cell in a highly alkaline electrolyte 0.1M KOH (pH=13). The roughness values are directly adapted from the authors reported capacitance measurements for OD-Cu ($\rho = 87$), and a Cu nanoflower ($\rho = 390$), while polycrystalline Cu foil in [26] is assumed as $\rho \approx 1$.

Data sets on Ac selectivity during CORR

The data sets shown in Figure 4 in the main text for acetate selectivity are adapted from [36, 37] and are both taken in comparable acetate promoting[1] conditions: Direct CO reduction in a gas-diffusion electrode/flow-cell setup in a highly alkaline electrolyte of 1.0 M KOH (pH=14).

In [36], Ji *et al.* compared nanoparticle (NP) shaped Cu, Pd, and Cu-Pd intermetallic and alloyed catalysts. The particles were synthesized following a uniform recipe (comparable shape and size) with different bulk (and thus surface) compositions. As shown in Fig. 4 in the main text and Supplementary figure 5, the Cu-Pd alloys show higher acetate selectivities as compared to the Cu-NP while Pd-NP (not shown) only exhibits HER activity rendering it inactive for CO_2RR. For all catalysts, roughness values were determined via capacitance measurements[36] which include the CORR-inactive Pd surface area that is not responsible for the re-adsorption and reduction of ketene. Therefore, we estimated the relative roughness based on the total current densities. This value is proportional to the electrocatalytically instead of the electrochemically active surface area (ECSA) and relevant for the catalytic selectivity. Both roughness values are depicted in Supplementary Table 3, labelled as ρ_C and ρ_j for capacitance and current density based estimates, respectively. Since no current densities for a planar catalyst (e.g. polycrystalline Cu) are available as a reference we need to scale the relative roughness values. We chose a factor of $m = 30$ which yields roughness dependent selectivity values that align with our model predictions as illustrated in Supplementary Figure 5. We note that this alignment does not reconcile ρ_C of Cu-NP with Cu foil from capacitance measurements in [36] (see Supplementary Table 3). This is due to the fact, that the Ac selectivity is, as a special case, not sensitive to catalyst loading but only to a micro- and

nanoscopic roughness due to an extremely short diffusion length[1]. The catalyst loading is, however, reflected in the current density leading to this inconsistency with capacitance based values.

The experiments by Sargent *et al.*[37] include Cu-Ag alloys to increase acetate selectivity. Using galvanic replacement, CuO_2 particles are only alloyed on their surface which explains the low but highly active alloying concentrations as compared to the Cu-Pd bulk alloys. No capacitance measurements to determine catalyst roughness were conducted or a reference planar catalyst was measured in this study. As shown in Supplementary Table 3, we therefore estimate relative roughness values from the total current densities as described in the Estimation of the catalyst roughness from measured current density Section. We scale the relative roughness values by a factor $m = 80$ to align the data with our model predictions in Supplementary Figure 5 and 4 in the main text.

Supplementary Table 3: Roughness values for the CuPd intermetallic (o-CuPd), the Cu-Pd alloys ($CuPd_{50\%}$, $CuPd_{23\%}$, and $CuPd_{77\%}$), derived from Cu Nanoparticles (Cu-NP)[36] as well as Cu-Ag alloys ($CuAg_{0.25-1\%}$) derived from Cu_2O NP[37]. The roughness values are estimated by capacitance measurements (ρ_C^{foil}) which are proportional to the electrochemically active surface area and estimated by the total current density (ρ_j^{rel}) which is proportional to the electrocatalytically active surface area. The relative ρ_j^{rel} are scaled by a factor $m = 30$ for Cu-Pd alloys and $m = 80$ for Cu-Ag alloys to match on the selectivity roughness curves in Supplementary Figure 5.

	ρ_C^{foil}	ρ_j^{rel}	$\rho_j^{\text{rel}} \times m$
o-CuPd	89.3	1.6 ± 0.2	47.0 ± 4.7
$CuPd_{50\%}$	353.1	1.6 ± 0.1	46.9 ± 2.0
$CuPd_{23\%}$	357.9	2.1 ± 0.0	61.8 ± 0.5
$CuPd_{77\%}$	419.3	1.0 ± 0.0	30.0 ± 0.0
Cu-NP	305.1	4.5 ± 0.5	135.6 ± 15.5
$CuAg_{0.25\%}$	-	1.0 ± 0.0	80.0 ± 0.0
$CuAg_{0.5\%}$	-	1.1 ± 0.0	91.6 ± 2.7
$CuAg_{1\%}$	-	1.1 ± 0.0	88.3 ± 2.2
Cu_2O	-	1.5 ± 0.1	117.8 ± 9.9

Visible in Supplementary Figure 5b and Figure 4 in the main text is a surprisingly close agreement between the model predictions and the alloy data, corroborating the facilitation of the desorption–re-adsorption-reaction mechanism through. A somewhat more prominent outlier is the $CuAg_{1.0\%}$ data point, which could indicate an additional electronic effect though alloying. Uncertainties in the total current density could, however, also explain deviation and further experimental characterization may be necessary to consolidate this finding.

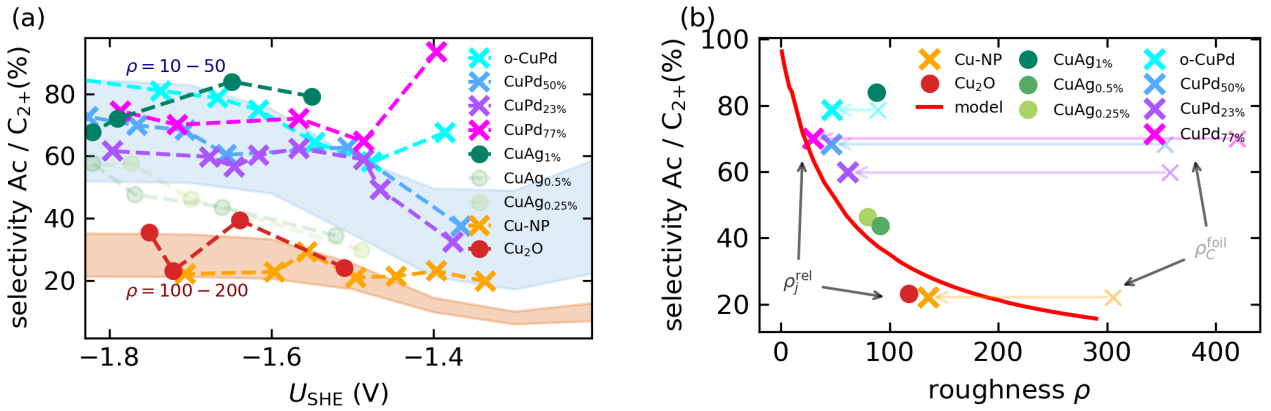

Supplementary Figure 5: Selectivity of Acetate among all C_{2+} products against potential vs. (a) U_{SHE}, (b) roughness ρ at -1.7 U_{SHE} including different estimates for ρ. The simulated data following a transport and solution reaction mediated mechanism[1] is shown for the roughness (ρ) ranges of 10-50 in light blue and 100-200 in red shades in (a) or as a solid red line in (b). The two ρ regimes in (a) serve as a guide to the eye, highlighting catalysts with high and low acetate selectivity, respectively. Note, that the complex potential dependence of the acetate selectivity is based on a more complex reaction mechanism of acetate formation that involves a solution reaction of ketene (the volatile product) with OH^- (generally also introducing a pH-dependence in addition to the here discussed ρ dependence)[1]. Shown are the experimentally measured selectivities for the CuPd intermetallic o-CuPd, the Cu-Pd alloys ($CuPd_{50\%}$, $CuPd_{23\%}$, and $CuPd_{77\%}$) which are derived from Cu Nanoparticles (Cu-NP) as adapted from [36] (dashed lines and crosses) and Cu-Ag alloys ($CuAg_{1\%}$, $CuAg_{0.5\%}$, $CuAg_{0.25\%}$) derived from Cu_2O particles as adapted from [37] (dashed lines and circles). Different roughness estimates shown in (b) are based on the total current density (ρ_j^{rel}) and on capacitance measurements[36] (ρ_C^{foil}, faded coloring). These roughness values correspond to the electrocatalytically active surface area and to the electrochemically active surface area, since the total current density is dominated by the CO_2RR activity of exposed Cu and the capacitive charging includes both Cu and the alloying metal. For ρ_j^{rel} values, a reference to planar Cu foil does not exists and it is therefore scaled by a relative factor m as shown in Supplementary Table 3.

Supplementary Note 3

Time-dependent Cu catalyst roughness during CO_2RR

Supplementary Figures 6 and 7 show time-dependent changes of relative catalyst roughness and CO selectivity against further reduced products of Cu-NP from the study by Huang *et al.*[38]. The data exemplifies the selectivity changes in CO_2RR due to catalyst aging. Overall, we find a decrease of roughness with time which correlates with an increasing CO selectivity against further reduced products in line with the desorption–re-adsorption-reaction mechanism.

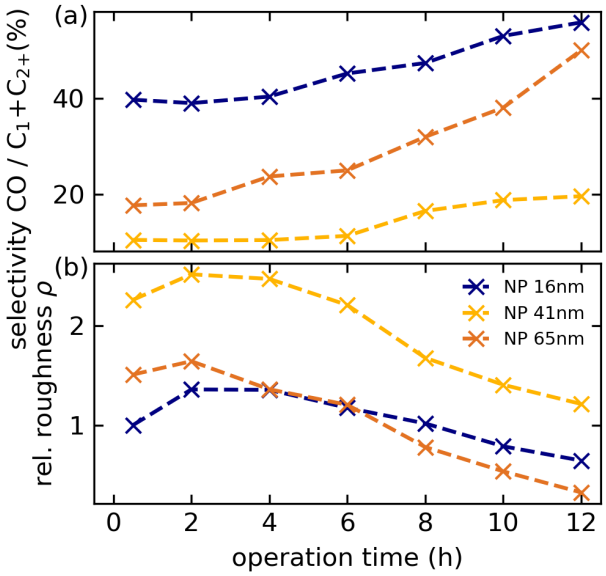

Supplementary Figure 6: (a) Selectivity for CO against further reduced products and (b) estimated relative roughness over the course of operation time for Cu-NP catalysts of different particle size. The experimental data is adapted from Huang *et al.*[38]. The relative roughness is estimated via the time dependent ethylene partial current density since total current densities are not available for all applied potentials. The ethylene current density is proportional to the CO_2RR relevant ECSA and we assume it comparable to the total current density (c.f. Supplementary Note 2).

For the sake of completeness, we note that CO selectivity in Supplementary Figure 6 does not always follow the trend that is expected from the changing catalyst morphology. This is, for example, the case during the first 2-4 hours of operation where an initial increase in ρ was attributed to particles' clustering (before their coalescence sets in). This is not accompanied, however, by a concomitant drop in CO selectivity (see arrows in Supplementary Figure 7). Many reasons could be responsible for this, including the creation of new active sites (such as e.g. steps and kinks) which may be inactive for the re-adsorption or further conversion of CO. Another inconsistency is the cross-over of the estimated roughness of 16 nm and 65 nm particles (blue and orange in Supplementary Figures 6 and 7) that is also not reflected in the selectivity, but which we attribute to an inaccuracy of our relative roughness estimation.

Time-dependent Pd catalyst roughness during ORR

The catalyst degradation related selectivity change due to the desorption–re-adsorption-reaction mechanism is not unique to CO_2RR on Cu. A similar phenomenon has been suggested as the origin of selectivity variations

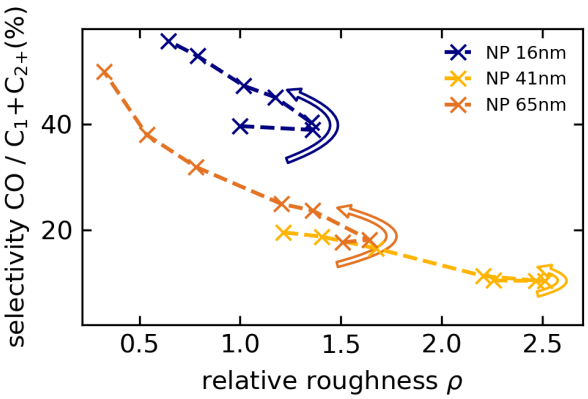

Supplementary Figure 7: Selectivity for CO against relative roughness for different Cu-NP. The data correspond to the time dependent data in Supplementary Figure 6 as adapted from Huang *et al.*[38]. The time dependence of the data is indicated by the arrows. The relative roughness is estimated via the time dependent ethylene partial current density which is proportional to the CO_2RR relevant ECSA (see Section on Estimation of the catalyst roughness from measured current density).

for ORR on Pd nanoparticles, where H_2O_2 yield was influenced by ECSA, which exhibited quantitative changes during voltage cycling[39]. Supplementary Figure 8a shows the ECSA decrease with increasing voltage cycles for Pd catalysts of different loadings. The influence of this ECSA decrease is illustrated in Supplementary Figure 8b, where a lower H_2O_2 yield is observed with higher ECSA. The values for ECSA and yields were taken from figures 6 and 7 as reported by Mittermeier *et al.*[39] where the ECSA had to be renormalized and yields were taken at the lowest potential ($\sim$ 0.1 U_{RHE}). Following this generality, we argue that the desorption–re-adsorption-reaction mechanism is highly instrumental in understanding the catalyst (de)activation with operation time for many applications.

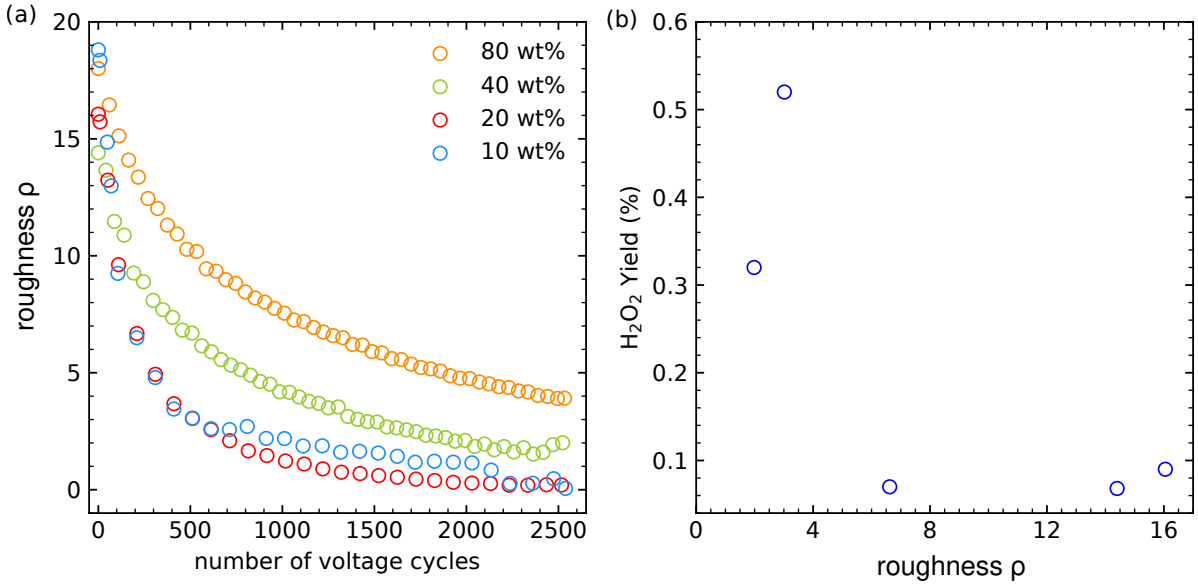

Supplementary Figure 8: (a) Roughness for Pd catalysts as a function of the number of voltage cycles at different catalyst loadings. (b) The H_2O_2 yield as a function of the palladium roughness at $\sim$ 0.1 U_{RHE}. The experimental data is adapted from Mittermeier *et al.*[39].

Supplementary References

1. Heenen, H. H. *et al.* The mechanism for acetate formation in electrochemical $CO_{(2)}$ reduction on Cu: selectivity with potential, pH, and nanostructuring. *Energy Environ. Sci.* **15,** 3978–3990 (2022).
2. Lausche, A. C. *et al.* On the effect of coverage-dependent adsorbate–adsorbate interactions for CO methanation on transition metal surfaces. *J. Catal.* **307,** 275–282 (2013).
3. Nørskov, J. *et al.* Origin of the Overpotential for Oxygen Reduction at a Fuel-Cell Cathode. *J. Phys. Chem. B* **108,** 17886–17892 (2004).
4. Kastlunger, G. *et al.* Using pH dependence to understand mechanisms in electrochemical CO reduction. *ACS Catal.* **12,** 4344–4357 (2022).
5. Virtanen, P. *et al.* SciPy 1.0: fundamental algorithms for scientific computing in Python. *Nat. Methods* **17,** 261–272 (2020).
6. Cussler, E. L. *Diffusion: mass transfer in fluid systems* (Cambridge university press, 2009).
7. Govindarajan, N., Kastlunger, G., Heenen, H. H. & Chan, K. Improving the intrinsic activity of electrocatalysts for sustainable energy conversion: where are we and where can we go? *Chem. Sci.* **13,** 14–26 (2022).
8. Treimer, S., Tang, A. & Johnson, D. C. A Consideration of the application of Koutecký-Levich plots in the diagnoses of charge-transfer mechanisms at rotated disk electrodes. *Electroanal.* **14,** 165–171 (2002).
9. Jang, J., Rüscher, M., Winzely, M. & Morales-Guio, C. G. Gastight rotating cylinder electrode: Toward decoupling mass transport and intrinsic kinetics in electrocatalysis. *AIChE J.* **68,** e17605 (2022).
10. Watkins, N. *et al.* Hydrodynamics Change Tafel Slopes in Electrochemical CO_2 Reduction on Copper. *ACS Energy Lett.* **8,** 2185–2192 (2023).
11. Marković, N. M., Gasteiger, H. A. & Ross, P. N. Oxygen Reduction on Platinum Low-Index Single-Crystal Surfaces in Alkaline Solution:Rotating Ring $Disk_{Pt(hkl)}$ Studies. *J. Phys. Chem.* **100,** 6715–6721 (1996).
12. Damjanovic, A., Genshaw, M. A. & Bockris, J. O. Distinction between Intermediates Produced in Main and Side Electrodic Reactions. *J. Chem. Phys.* **45,** 4057–4059 (Dec. 1966).
13. Peterson, A. A., Abild-Pedersen, F., Studt, F., Rossmeisl, J. & Nørskov, J. K. How copper catalyzes the electroreduction of carbon dioxide into hydrocarbon fuels. *Energy Environ. Sci.* **3,** 1311–1315 (2010).
14. Heenen, H. H., Gauthier, J. A., Kristoffersen, H. H., Ludwig, T. & Chan, K. Solvation at metal/water interfaces: An ab initio molecular dynamics benchmark of common computational approaches. *J. Chem. Phys.* **152,** 144703 (2020).
15. Gauthier, J. A. *et al.* Unified approach to implicit and explicit solvent simulations of electrochemical reaction energetics. *J. Chem. Theory Comput.* **15,** 6895–6906 (2019).
16. Beinlich, S. D., Hörmann, N. G. & Reuter, K. Field Effects at Protruding Defect Sites in Electrocatalysis at Metal Electrodes? *ACS Catal.* **12,** 6143–6148 (2022).

17. Dudzinski, A. M., Diesen, E., Heenen, H. H., Bukas, V. J. & Reuter, K. First Step of the Oxygen Reduction Reaction on Au(111): A Computational Study of O_2 Adsorption at the Electrified Metal/Water Interface. *ACS Catal.* **13,** 12074–12081 (2023).

18. O'Sullivan, D. W., Lee, M., Noone, B. C. & Heikes, B. G. Henry's law constant determinations for hydrogen peroxide, methyl hydroperoxide, hydroxymethyl hydroperoxide, ethyl hydroperoxide, and peroxyacetic acid. *J. Phys. Chem.* **100,** 3241–3247 (1996).

19. Katsounaros, I. *et al.* Hydrogen peroxide electrochemistry on platinum: towards understanding the oxygen reduction reaction mechanism. *Phys. Chem. Chem. Phys.* **14,** 7384–7391 (2012).

20. Kelly, S. R., Kirk, C., Chan, K. & Nørskov, J. K. Electric field effects in oxygen reduction kinetics: rationalizing pH dependence at the Pt (111), Au (111), and Au (100) electrodes. *J. Phys. Chem. C* **124,** 14581–14591 (2020).

21. Allou, L., El Maimouni, L. & Le Calvé, S. Henry's law constant measurements for formaldehyde and benzaldehyde as a function of temperature and water composition. *Atmos. Environ.* **45,** 2991–2998 (2011).

22. Gharagheizi, F. Determination of diffusion coefficient of organic compounds in water using a simple molecular-based method. *Ind. Eng. Chem. Res* **51,** 2797–2803 (2012).

23. Sander, R. Compilation of Henry's law constants (version 4.0) for water as solvent. *Atmos. Chem. Phys* **15,** 4399–4981 (2015).

24. Staudinger, J. & Roberts, P. V. A critical compilation of Henry's law constant temperature dependence relations for organic compounds in dilute aqueous solutions. *Chemosphere* **44,** 561–576 (2001).

25. Mansfield, M. L. Mass Transport of Gases across the Air–Water Interface: Implications for Aldehyde Emissions in the Uinta Basin, Utah, USA. *Atmosphere* **11,** 1057 (2020).

26. Kuhl, K. P., Cave, E. R., Abram, D. N. & Jaramillo, T. F. New insights into the electrochemical reduction of carbon dioxide on metallic copper surfaces. *Energy Environ. Sci.* **5,** 7050–7059 (2012).

27. Nitopi, S. *et al.* Progress and perspectives of electrochemical CO_2 reduction on copper in aqueous electrolyte. *Chem. Rev.* **119,** 7610–7672 (2019).

28. Limaye, A. M., Zeng, J. S., Willard, A. P. & Manthiram, K. Bayesian data analysis reveals no preference for cardinal Tafel slopes in CO_2 reduction electrocatalysis. *Nat. Commun.* **12,** 703 (2021).

29. Seidel, Y. *et al.* Mesoscopic mass transport effects in electrocatalytic processes. *Faraday Discuss.* **140,** 167–184 (2009).

30. Jusys, Z., Kaiser, J. & Behm, R. Methanol electrooxidation over Pt/C fuel cell catalysts: dependence of product yields on catalyst loading. *Langmuir* **19,** 6759–6769 (2003).

31. Li, C. W. & Kanan, M. W. CO_2 reduction at low overpotential on Cu electrodes resulting from the reduction of thick Cu_2O films. *J. Am. Chem. Soc.* **134,** 7231–7234 (2012).

32. Huang, Y., Handoko, A. D., Hirunsit, P. & Yeo, B. S. Electrochemical reduction of CO_2 using copper single-crystal surfaces: effects of CO* coverage on the selective formation of ethylene. *ACS Catal.* **7,** 1749–1756 (2017).

33. Bertheussen, E. *et al.* Electroreduction of CO on polycrystalline copper at low overpotentials. *ACS Energy Lett.* **3,** 634–640 (2018).

34. Bertheussen, E. *et al.* Acetaldehyde as an intermediate in the electroreduction of carbon monoxide to ethanol on oxide-derived copper. *Angew. Chem. Int. Ed.* **128,** 1472–1476 (2016).

35. Wang, L. *et al.* Electrochemically converting carbon monoxide to liquid fuels by directing selectivity with electrode surface area. *Nat. Catal.* **2,** 702–708 (2019).

36. Ji, Y. *et al.* Selective CO-to-acetate electroreduction via intermediate adsorption tuning on ordered Cu–Pd sites. *Nat. Catal.* **5,** 251–258 (2022).

37. Dorakhan, R. *et al.* A silver–copper oxide catalyst for acetate electrosynthesis from carbon monoxide. *Nat. Synth.* **2,** 448–457 (2023).

38. Huang, J. *et al.* Potential-induced nanoclustering of metallic catalysts during electrochemical CO_2 reduction. *Nat. Commun.* **9,** 3117 (2018).

39. Mittermeier, T., Weiß, A., Gasteiger, H. A. & Hasché, F. Monometallic palladium for oxygen reduction in PEM fuel cells: particle-size effect, reaction mechanism, and voltage cycling stability. *J. Electrochem. Soc.* **164,** F1081 (2017).